11th International Symposium on Plasticity and Impact Mechanics, Implast 2016

Effective Constitutive Response of Sustainable Next Generation Infrastructure Materials through High-Fidelity Experiments and Numerical Simulation

Sumanta Das[a]*, Xianghui Xiao[b], Nikhilesh Chawla[c], Narayanan Neithalath[d]

[a]Civil & Environmental Engineering, University of Rhode Island, Kingston, RI 02881, USA
[b]Advanced Photon Source, Argonne National Laboratory, Lemont, IL 60439, USA
[c]Materials Science and Engineering, Arizona State University, Tempe, AZ 85281, USA
[d] School of Sustainable Engineering and the Built Environment, Arizona State University, Tempe, AZ 85281, USA

Abstract

Design of novel infrastructure materials requires a proper understanding of the influence of microstructure on the desired performance. The priority is to seek new and innovative ways to develop sustainable infrastructure materials using natural resources and industrial solid wastes in a manner that is ecologically sustainable and yet economically viable. Structural materials are invariably designed based on mechanical performance. Accurate prediction of effective constitutive behavior of highly heterogeneous novel structural materials with multiple microstructural phases is a challenging task. This necessitates reliable classification and characterization of constituent phases in terms of their volume fractions, size distributions and intrinsic elastic properties, coupled with numerical homogenization technique. This paper explores a microstructure-guided numerical framework that derives inputs from nanoindentation and synchrotron x-ray tomography towards the prediction of effective constitutive response of novel sustainable structural materials so as to enable microstructure-guided design.

* Corresponding author. Tel.: +1-401-874-5637
  E-mail address: sumanta_das@uri.edu

1. Introduction

Understanding the microstructure-mechanical property relationship is critical towards design and development of heterogeneous composites. Prediction of effective elastic property of highly heterogeneous materials with several phases is a challenging task. Accurate effective property prediction necessitates selection of appropriate homogenization method, accurate characterization and classification of component phases in terms of their volume fraction, size distribution and intrinsic elastic property.

Prediction of effective constitutive property of heterogeneous materials has been traditionally attained using different analytical techniques that deal with only volume fraction of phases [1,2]. However, these analytical/semi-analytical methods only give estimates of bounds for the macroscopic properties. Furthermore, these techniques have been proved to be insufficient when the stiffness –contrast among component phases is large or when large inclusion volume fractions are incorporated [3,4]. Over the past few decades, the computational methods for homogenization have been an active area of research and tremendous improvement has been achieved in terms of computational efficiency. Through these developments over the years, finite element method (FEM) has been established as one of the most efficient numerical approaches to predict macroscopic behavior by volumetrically averaging numerical results obtained for representative volume elements (RVE). This microstructure-guided numerical homogenization scheme eliminates the shortcomings of the analytical schemes and thus yields a better solution. But, accuracy of predicted results depends on size of RVE and choice of appropriate microscopic boundary condition. In addition, realistic representation of microstructural features and component material properties is also required. The microstructure can be generated artificially using statistical information [3,5,6] or actual 3D tomography image can be used [3,7,8]. While the former approach can be implemented with reasonable degree of accuracy [5,6], implementation of microstructure, obtained from tomography, through a voxel-based discretization approach becomes computationally demanding. The voxel-based approach introduces distortions at the phase-interfaces and thus induces artificial anisotropy, which would necessitate significantly large number of elements in order to obtain a converged solution.

This paper presents an effective property prediction approach through synergistic application of synchrotron x-ray tomography, nanoindentation and numerical homogenization involving finite element analysis. The methodology involves: (1) generation of a representative volume element (RVE) of the heterogeneous material using a microstructural stochastic packing algorithm based on actual microstructural features extracted using modern imaging techniques such as high resolution 3D synchrotron x-ray tomography, (2) implementation of accurate intrinsic elastic property of component phases in the microstructure, obtained from statistical nanoindentation technique, (3) application of periodic boundary condition in the RVE and finite element analysis to simulate a strain-controlled test-scenario and (4) obtain effective volume-averaged RVE stress/strains or effective homogenized Young's modulus of the material through a homogenization module. The approach is applied on fly-ash based geopolymers [9–11] in this paper. The current work is intended to link the macroscopic elastic property of the novel heterogeneous materials with its microstructure with a view to build a tool for efficient design of novel random heterogeneous cementitious materials for various applications.

2. Micromechanical Modelling for Effective Constitutive Response of Heterogeneous Cementitious Composites

This section describes the microstructure-guided constitutive modelling framework for heterogeneous composites. The framework, explained herein, executes multi-scale analysis of heterogeneous composites involving generation of unit cell based on known inclusion size distributions, meshing of unit cell, application of appropriate boundary conditions and stress analysis using a commercial finite element solver. The detailed procedure is explained in the following sections.

2.1. Generation of representative volume element (RVE)

Generation of RVE is accomplished here using Lubachhevsky-Stillinger algorithm [12]. The algorithm uses hard contact model and hence particle overlap is not allowed. Here, the RVE is set to be a cube. First, the desired

number of particles are randomly distributed inside the periodic bounding box with random initial velocities of the particles. The radius of each particle is initialized at zero. The radius of ith particles in the next event is then increased with different growth rates:

$$\frac{dr_i}{dt} = g_i \tag{1}$$

Where $I = 1, 2,\ldots$, number of particles. The growth rate of different particles is controlled so as to attain the desired particle size distribution. The growth rate in between time t^n and t^{n+1} are computed using finite difference scheme as follows:

$$g_i = \frac{(r_i^{n+1} - r_i^n)}{\Delta t} \tag{2}$$

The particle radii are updated as follows for time t^{n+1}:

$$r_i^{n+1} = r_i^n + g_i \Delta t \tag{3}$$

Now, the position of particle 'i' at time t^{n+1} is updated considering a constant velocity between the time nodes:

$$x_i^{n+1} = x_i^n + v_i^n \Delta t \tag{4}$$

The vector that connects centers of particles 'i' and 'j' is obtained by subtracting position vectors of the two particles:

$$I_{ij}^{n+1} = x_j^{n+1} - x_i^{n+1} \tag{5}$$

The particles 'i' and 'j' are in contact if the sum of their radii is equal to the length of the connection vector. The time step size can be calculated as:

$$\Delta t = \min\left[\frac{-V \pm \sqrt{V^2 - UW}}{U}\right] \tag{6}$$

Where $\Delta t > 0$ and V, U and W are given as:

$$V = I_{ij}^n \cdot [v_j^n - v_i^n] - [r_i^n + r_j^n][g_i + g_j] \tag{7a}$$

$$U = [v_j^n - v_i^n]^2 - [g_i + g_j]^2 \tag{7b}$$

$$W = [I_{ij}^n]^2 - [r_i^n + r_j^n]^2 \tag{7c}$$

This time step calculation (Equation 6) is performed for each particle pair that are being able to collide and thus minimum time step for all the possible collisions is adopted to move forward for the next event. All the particle positions x_i^{n+1} are updated using forward Euler scheme (Equation 4) and new search for next collision is started. The post-contact velocities are computed as follows:

$$v_{n_i}^{n+1^+} = \min\{v_{n_i}^{n+1^-}, v_{n_j}^{n+1^-}\} - g_i \quad ; \quad v_{n_j}^{n+1^+} = \max\{v_{n_i}^{n+1^-}, v_{n_j}^{n+1^-}\} + g_i \tag{8}$$

Thus, all the above-mentioned steps are repeated and in the process of iterations the particles change position in the bounding box, collide and grow in order to obtain desired volume fraction. Finally, the obtained microstructural information is implemented through a python language script to enable it to be imported to finite element software such as ABAQUS^{TM}.

2.2. Boundary conditions

Choice of appropriate microscopic boundary condition is an essential step in any numerical homogenization method. In this work, periodic boundary condition is adopted since it has been shown to provide better approximation of effective property of heterogeneous materials than in the case of uniform boundary condition even

if the microstructure does not have actual geometrical periodicity [13,14]. Periodic boundary condition ensures two continuity criteria at the boundaries of neighbouring unit cells in order to ensure assembly of individual unit cells as a physical continuous body [15]: (i) displacement continuity, i.e., neighbouring unit cells cannot be separated or they cannot penetrate each other; and (ii) traction continuity at the boundary of neighbouring unit cells. The displacement field in any 2D periodic microstructure is given as [15]:

$$v_i(x_1, x_2) = \varepsilon_{ij}^0 x_j + v_i^*(x_1, x_2) \tag{9}$$

Here, ε_{ij}^0 is the applied strain tensor, and v_i^* is a periodic function representing the modification of linear displacement field due to the heterogeneous microstructure. For, the unit cell shown in Figure 1(b), the displacements on a pair of parallel opposite boundary edges are given as:

$$v_i^{s+} = \varepsilon_{ij}^0 x_j^{s+} + v_i^* \tag{10a}$$

$$v_i^{s-} = \varepsilon_{ij}^0 x_j^{s-} + v_i^* \tag{10b}$$

Here, s^+ and s^- are s^{th} pair of two opposite parallel boundary surfaces of the unit cell as shown in Figure 1(b). The periodic function v^* is the same at both the parallel opposite edges due to periodicity. The difference between the displacement fields of the two opposite parallel boundary edges is given as:

$$v_i^{s+} - v_i^{s-} = \varepsilon_{ij}^0 (x_j^{s+} - x_j^{s-}) = \varepsilon_{ij}^0 \Delta x_j^s \tag{11}$$

For a pair of opposite parallel boundary edges, Δx_j^s is constant for a specified ε_{ij}^0. The perturbation is introduced to the system of equation through a reference node which only acts as a carrier for the load and is not attached to any element in the model. The general form of complete set of equations can be written as:

$$v_i^{s+} - v_i^{s-} + v_i^{dummy} = 0 \tag{12}$$

2.3. Finite element simulation and numerical homogenization

The RVE is meshed through the python script and the analysis is implemented through ABAQUS™ solver. Thus this approach simulates a strain- (or displacement) controlled test scenario. To efficiently handle post-processing of the simulated individual element stresses, a homogenization module is developed to obtain effective volume-averaged RVE stresses/strains. The effective stresses are computed against different applied strains and thus, the effective constitutive relationship is obtained.

3. Experimental Program to derive input for numerical simulation

3.1. Materials and Mixture Proportions

A Class F fly ash conforming to ASTM C 618 was used as the starting material for synthesis of alkali-activated fly ash (AAFA) geopolymer. 8M NaOH solution was used to activate the fly ash. The alkaline solution was added to fly ash, and mixed for 4 minutes in a laboratory mixer. The mixtures were then filled in molds and subjected to heat curing in a laboratory oven at 60°C for 48 hours, in sealed conditions. This curing process was previously shown to provide a compressive strength of 25-30 MPa [10], which is commonly adopted for many types of structural concretes.

3.2. Synchrotron x-ray Tomography

Synchrotron X-ray tomography (XRT) was performed at the 2 BM beamline of the Advanced Photon Source (APS) at Argonne National Laboratory. Details of APS beamline 2 BM have been described elsewhere [16,17]. XRT has been employed in the analysis of pore-structure of cementitious materials and synchrotron

microtomography is considered highly suitable for the evaluation of pore structure that is influential in dictating the bulk mechanical behavior of the [18–21].

3.3. Nanoindentation

For nanoindentation test on geopolymer, a cylindrical sample of 25 mm in diameter and 75 mm in height was prepared and heat cured at 60°C for 48 hours. A cubical piece of 4 mm side length was cut from the core of the sample using a diamond saw. The sample was then encapsulated using a two-part epoxy and vacuum impregnated at 95 KPa followed by an overnight cure at room temperature. Coarse grinding steps were accomplished using silicon carbide (SiC) abrasive discs to planarize and remove deformations caused by sectioning. Successive polishing steps were carried out using smaller sized abrasives, and completed using 0.04 µm colloidal silica suspension to ensure a very smooth surface. The nanoindentation measurements were carried out on the polished sample in a commercial Nanoindenter (Nanoindenter XP-II, Agilent) using a Berkovich tip. Indentations were carried out at initially at 10 µm spacing in a grid on an area approximately 250 µm x 250 µm in size. All the indentation locations were carefully selected prior to testing to ensure that the pores or cavities are not encountered in the process. Thus the indentation experiments were carried out mostly only on the solid phases, which resulted in no spurious peaks in the modulus frequency distribution curves. Continuous stiffness measurement (CSM) technique [22,23] was employed here to measure the Young's modulus of phases.

4. Effective Constitutive Response of Fly Ash Geopolymer

The current numerical constitutive modelling framework has been applied to alkali activated fly ash geopolymers in order to verify the efficacy of the method to determine the macro-scale Young's modulus through synergistic use of high fidelity experiments such as nanoindentation, synchrotron XRT coupled with numerical homogenization technique.

4.1. 3D Characterization and quantification of component phases using Synchrotron X-Ray Tomography (XRT)

Figure 1(a) shows a representative cubic volume of interest of the fly ash geopolymer obtained from reconstruction of synchrotron XRT images. Figure 1(b) shows the pore (red) and solid (grey) phases segmented using transition point-based thresholding coupled with the application of appropriate discrete thresholding in the microstructure to obtain the most realistic representation of known microstructural features. The segmentation procedure is described in detail in [9]. Figure 1(c) shows segmented pore, unreacted and pertly reacted fly ash and NASH gel. Here, the unreacted fly ash particles are not separable from partially reacted ones due to lack of sufficient absorption contrast between these phases. Thus synchrotron XRT is used to quantify the pore structure alone in this study. The AAFA shows a segmented porosity of 32%. XRT dataset shows that pores in the size range of 0.74 µm-to-50 µm and the pores in the size range of 5 µm-to-25 µm contribute the most to the overall segmented porosity.
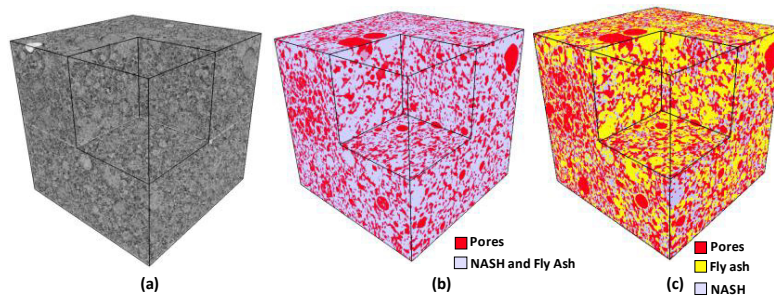

Fig. 1: Sequential, discrete thresholding implemented on a 3003 voxel RVE obtained from XRT: (a) original XRT image, (b) 3D image after pore segmentation (two-phase; pore and solid), and (c) 3D image after further segmentation for two different solid phases (fly ash and N-A-S-H gel).

4.2. Phase properties using nanoindentation

The intrinsic elastic property of component phases in the fly ash geopolymer is classified and quantified using statistical nanoindentation. Different component phases are identified through microstructural observations. The phase-identification process is detailed in [9]. Figure 2(a) and (b) shows the load-penetration depth responses and Young's modulus as a function of penetration depth respectively for four distinctively identified phases. Figure 2(c) shows the peaks obtained through statistical deconvolution [24,25] of the histogram. Four characteristic peaks are observed in the histogram. The peaks were assigned to different solid phases based on microstructural observation. The phase with the highest elastic modulus is attributed to the unreacted fly ash present in the matrix, while the phase with the lowest elastic modulus is attributed to the N-A-S-H gel phase that is formed through diffusion of the ionic species and gel precipitation in the empty spaces in the microstructure. The peak corresponding to the lower among the remaining two peaks corresponds to the fly ash particles that have reacted partially. The remaining peak could be attributed to particles with some reaction products on the surface, or to unreacted fly ash particles with cavities, as observed in the microstructure. The nanoindentation results are reported in detail in [9]. For simplification, partially activated fly ash is homogenized with the N-A-S-H gel (which is the major reaction product in fly ash-based geopolymers) using the Mori-Tanaka method [1].
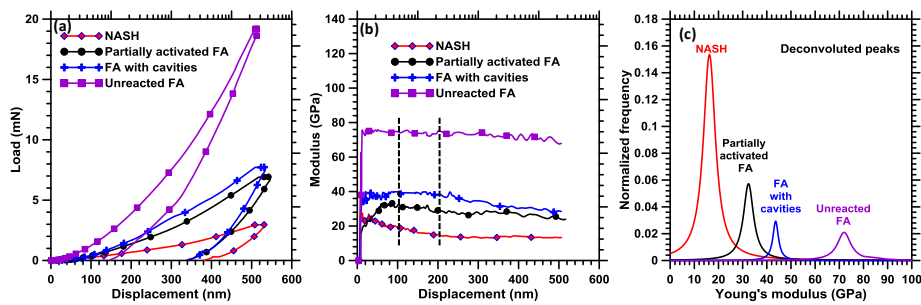

Fig. 2: (a) Load-penetration depth curves, (b) Elastic modulus as a function of the penetration depth for the four distinct solid phases; and (c) deconvoluted component peaks for the four distinctly identifiable microstructural phases in the solid component of the paste. The area under each deconvoluted peak is the fraction of that respective solid phase in all solids in the paste.

Furthermore, fly ash particles with cavities and the unreacted fly ash particles are homogenized together. Thus, pores, unreacted fly ash (including those with cavities) and the matrix (partially activated fly ash homogenized with the N-A-S-H gel) are used as the different microstructural phases in numerical simulation. The size distribution of unreacted fly ash (starting material) as obtained from laser diffraction [9] is used in numerical simulation.

4.3. Two-step Numerical Homogenization for Effective property prediction

Two-stage numerical homogenization is performed to obtain homogenized Young's modulus of the geopolymer. In Stage-I, the unreacted fly ash particles are homogenized with the matrix. Figure 3(a) shows the 3D microstructure containing fly ash (green) and the matrix (blue) phases. The RVE is meshed with tetrahedral C3D10 elements (in ABAQUS™) and periodic boundary conditions are implemented as explained earlier. Figure 3(b) shows the dominant principal stress distribution in the RVE corresponding to an externally applied strain of 0.12%. The constitutive relationship thus obtained after the application of different strains is shown in Figure 3(c). In Stage-II, the homogenized value from Stage-I is used as the elastic modulus of the matrix, and the pores are incorporated into the microstructure (Figure 4(a)). Figure 4(b) shows the dominant principal stress distribution in the unit cell when an externally applied strain of 0.1% is applied. The constitutive relationship for the fly ash geopolymer is shown in Figure 4(c). The numerically homogenized value of 15.6 GPa correlates well with the experimentally obtained (three-point bending test) Young's modulus of 14.73 ± 0.7 GPa.
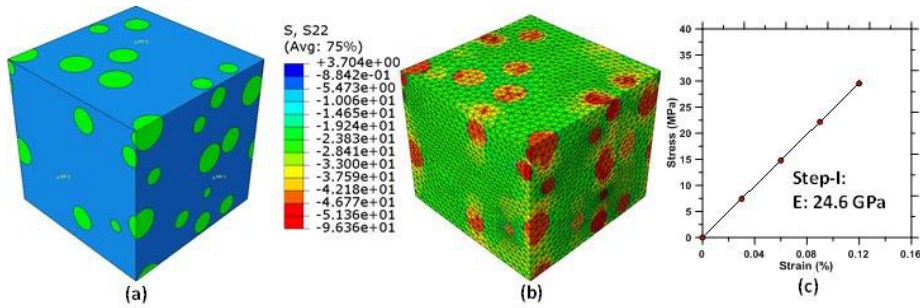
Fig. 3: Step-I: (a) FE model showing the unreacted fly ash and matrix; (b) stress distribution (MPa) under an imposed strain of 0.12%, and (c) the constitutive relationship in the linear elastic regime
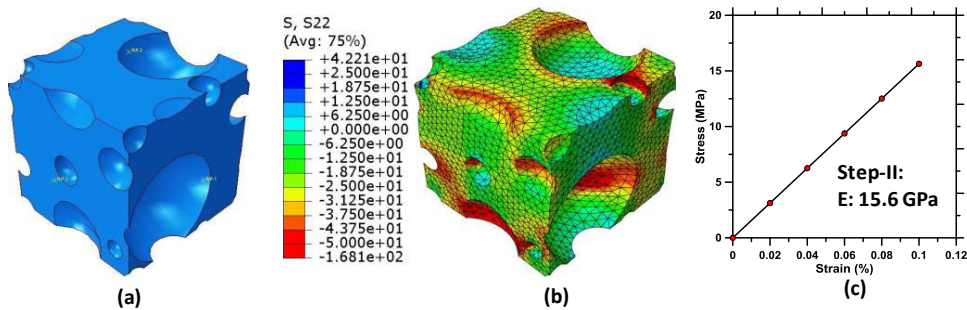

Fig. 4: Stage-II: (a) FE model showing the matrix (from Stage-I) and the pores; (b) stress distribution (MPa) under a strain of 0.1%, and (c) the constitutive relationship in the linear elastic regime

5. Conclusions

Good agreement between the predicted and experimental Young's modulus for geopolymers presented here provides confidence on the ability of the current methodology to be applied for many classes of highly heterogeneous novel sustainable infrastructure materials. This study thus links the microstructure with the macro-scale effective mechanical behavior of highly heterogeneous materials enabling efficient design strategies to tailor the microstructure for requisite mechanical performance of highly heterogeneous infrastructure materials.

Acknowledgements

References

[1]   T. Mori, K. Tanaka, Average stress in matrix and average elastic energy of materials with misfitting inclusions, Acta Metall. 21 (1973) 571–574.
[2]   M. Hori, S. Nemat-Nasser, Double-inclusion model and overall moduli of multi-phase composites, Mech. Mater. 14 (1993) 189–206.
[3]   C.F. Dunant, B. Bary, A.B. Giorla, C. Péniguel, J. Sanahuja, C. Toulemonde, A.-B. Tran, F. Willot, J. Yvonnet, A critical comparison of several numerical methods for computing effective properties of highly heterogeneous materials, Adv. Eng. Softw. 58 (2013) 1–12.
[4]   M.I. Idiart, F. Willot, Y.-P. Pellegrini, P. Ponte Castañeda, Infinite-contrast periodic composites with strongly nonlinear behavior: Effective-medium theory versus full-field simulations, Int. J. Solids Struct. 46 (2009) 3365–3382.
[5]   I. Comby-Peyrot, F. Bernard, P.-O. Bouchard, F. Bay, E. Garcia-Diaz, Development and validation of a 3D computational tool to describe concrete behaviour at mesoscale. Application to the alkali-silica reaction, Comput. Mater. Sci. 46 (2009) 1163–1177.

[6]   C.F. Dunant, K.L. Scrivener, Micro-mechanical modelling of alkali–silica-reaction-induced degradation using the AMIE framework, Cem. Concr. Res. 40 (2010) 517–525.

[7]   J. Escoda, F. Willot, D. Jeulin, J. Sanahuja, C. Toulemonde, Estimation of local stresses and elastic properties of a mortar sample by FFT computation of fields on a 3D image, Cem. Concr. Res. 41 (2011) 542–556.

[8]   M. Hain, P. Wriggers, Computational homogenization of micro-structural damage due to frost in hardened cement paste, Finite Elem. Anal. Des. 44 (2008) 233–244.

[9]   S. Das, P. Yang, S.S. Singh, J.C.E. Mertens, X. Xiao, N. Chawla, N. Neithalath, Effective properties of a fly ash geopolymer: Synergistic application of X-ray synchrotron tomography, nanoindentation, and homogenization models, Cem. Concr. Res. 78 (2015) 252-262.

[10]   D. Ravikumar, S. Peethamparan, N. Neithalath, Structure and strength of NaOH activated concretes containing fly ash or GGBFS as the sole binder, Cem. Concr. Compos. 32 (2010) 399–410.

[11]   M. Chi, R. Huang, Binding mechanism and properties of alkali-activated fly ash/slag mortars, Constr. Build. Mater. 40 (2013) 291–298.

[12]   B.D. Lubachevsky, F.H. Stillinger, Geometric properties of random disk packings, J. Stat. Phys. 60 (1990) 561–583.

[13]   K. Terada, M. Hori, T. Kyoya, N. Kikuchi, Simulation of the multi-scale convergence in computational homogenization approaches, Int. J. Solids Struct. 37 (2000) 2285–2311.

[14]   O. van der Sluis, P.J.G. Schreurs, W.A.M. Brekelmans, H.E.H. Meijer, Overall behaviour of heterogeneous elastoviscoplastic materials: effect of microstructural modelling, Mech. Mater. 32 (2000) 449–462.

[15]   P. Suquet, Elements of homogenization for inelastic solid mechanics, (1987).

[16]   J.J. Williams, Z. Flom, A.A. Amell, N. Chawla, X. Xiao, F. De Carlo, Damage evolution in SiC particle reinforced Al alloy matrix composites by X-ray synchrotron tomography, Acta Mater. 58 (2010) 6194–6205.

[17]   F. De Carlo, B. Tieman, High-throughput x-ray microtomography system at the Advanced Photon Source beamline 2-BM, in: 2004: pp. 644–651.

[18]   J.L. Provis, R.J. Myers, C.E. White, V. Rose, J.S.J. van Deventer, X-ray microtomography shows pore structure and tortuosity in alkali-activated binders, Cem. Concr. Res. 42 (2012) 855–864.

[19]   N. Bossa, P. Chaurand, J. Vicente, D. Borschneck, C. Levard, O. Aguerre-Chariol, J. Rose, Micro- and nano-X-ray computed-tomography: A step forward in the characterization of the pore network of a leached cement paste, Cem. Concr. Res. 67 (2015) 138–147.

[20]   M. Zhang, Y. He, G. Ye, D.A. Lange, K. van Breugel, Computational investigation on mass diffusivity in Portland cement paste based on X-ray computed microtomography (μCT) image, Constr. Build. Mater. 27 (2012) 472–481.

[21]   P.J.M. Monteiro, A.P. Kirchheim, S. Chae, P. Fischer, A.A. MacDowell, E. Schaible, H.R. Wenk, Characterizing the nano and micro structure of concrete to improve its durability, Cem. Concr. Compos. 31 (2009) 577–584.

[22]   W. c. Oliver, G. m. Pharr, Measurement of hardness and elastic modulus by instrumented indentation: Advances in understanding and refinements to methodology, J. Mater. Res. 19 (2004) 3–20.

[23]   X. Li, B. Bhushan, A review of nanoindentation continuous stiffness measurement technique and its applications, Mater. Charact. 48 (2002) 11–36.

[24]   G. Constantinides, K.S. Ravi Chandran, F.-J. Ulm, K.J. Van Vliet, Grid indentation analysis of composite microstructure and mechanics: Principles and validation, Mater. Sci. Eng. A 430 (2006) 189–202.

[25]   J. Němeček, V. Šmilauer, L. Kopecký, Nanoindentation characteristics of alkali-activated aluminosilicate materials, Cem. Concr. Compos. 33 (2011) 163–170.